Effects of Microphysical Latent Heating on the Rapid Intensification of Typhoon Hato (2017)

Dajun ZHAO[1,2], Yubin YU[1,3*], Jinfang YIN[1], and Hongxiong XU[1]

1 *State Key Laboratory of Severe Weather*, *Chinese Academy of Meteorological Sciences*, *China Meteorological Administration*, *Beijing* 100081
2 *University of Chinese Academy of Sciences*, *Beijing* 100049
3 *China Meteorological Administration*, *Beijing* 100081

(Received May 13, 2019; in final form December 7, 2019)

ABSTRACT

A 72-h cloud-resolving numerical simulation of Typhoon Hato (2017) is performed by using the Weather Research and Forecasting (WRF) model with the Advanced Research WRF (ARW) core (V3.8.1) on a horizontal resolution of 2 km. To enhance the background tropical cyclone structure and intensity, a vortex dynamic initialization scheme with a terrain-filtering algorithm is utilized. The model reproduces reasonably well the track, structure, and intensity change of Typhoon Hato. More specifically, the change trend of simulated maximum wind speed is consistent with that of best-track analysis, and the simulated maximum wind of 49 m s^{-1} is close to that (52 m s^{-1}) of the best-track analysis, indicating that the model has successfully captured the rapid intensification (RI) of Typhoon Hato (2017). Analyses of the model outputs reveal that the total microphysical latent heating of the inner-core region associated with enhanced vertical upward motion reaches its maximum at 9-km height in the upper troposphere during the RI stage. The dominant microphysical processes with positive latent heat contributions (i.e., heating effect) are water vapor condensation into cloud water (67.6%), depositional growth of ice (12.9%), and generation (nucleation) of ice from vapor (7.9%). Those with negative latent heat contributions (cooling effect) are evaporation of rain (47.6%), melting of snow (27.7%), and melting of graupel (9.8%). Sensitivity experiments further show that the intensification speed and peak intensity of this typhoon are highly correlated to the dominant heating effect. A significant increase in graupel over 5–10-km height and snow at 10–14-km height in the inner-core region of Typhoon Hato corresponds well with its RI stage, and the latent heating from nucleation and depositional growth is crucial to the RI of simulated Hato.

Key words: microphysical latent heating, rapid intensification, typhoon, budget analysis

Citation: Zhao, D., Y. B. Yu, J. F. Yin, et al., 2020: Effects of microphysical latent heating on the rapid intensification of Typhoon Hato (2017). *J. Meteor. Res.*, **34**(2), 368–386, doi: 10.1007/s13351-020-9076-z.

1. Introduction

Great progress has been made in forecasting of tropical cyclone (TC) tracks in the past several decades. However, the forecasting skill with respect to TC intensity has only improved slowly, especially in terms of the offshore rapid intensification (RI) of TCs. TC RI is usually defined as an intensifying rate of more than 42 hPa day^{-1} in the minimum pressure (Holliday and Thompson, 1979) or 15 m s^{-1} day^{-1} in the surface maximum tangential wind (Kaplan and DeMaria, 2003). It is generally believed that TC RI occurs under favorable environmental conditions such as higher sea surface temperature, a deeper warm-water mixed layer, smaller vertical wind shear, higher relative humidity in the lower and middle troposphere, and a favorable high-altitude trough (Wang and Wu, 2004; Leroux et al., 2013; Kaplan et al., 2015). Previous studies have revealed that vertical hot towers (Houze, 2010) and convective bursts play significant roles in RI. Additionally, some critical mechanisms involved are the increase in mass convergence produced by convective downdrafts (Rogers, 2010), strong deep convection occurring inside the radius of maximum wind (RMW; Wang and Wang, 2014), the development of up-

Supported by the National Natural Science Foundation of China (41775048) and National Key Research and Development Program of China (2017YFC1501602).

*Corresponding author: yuyb@cma.gov.cn.

per-level warming in the eye (Chen and Gopalakrishnan, 2015), and a symmetric convective structure (Miyamoto and Nolan, 2018). Although much research has been carried out (Heng et al., 2017; Tao et al., 2017; Liu et al., 2018a, b; Qin et al., 2018), the mechanism of TC RI is still one of the most important and challenging questions in TC research and operational forecasting.

Diabatic heating is the main energy source for the development of a TC; in particular, latent heating plays an important role in TC intensity change (Anthes, 1982). Based on balanced vortex theory, Schubert and Hack (1982) and Vigh and Schubert (2009) showed that when the latent heating is located within the region of enhanced inertial stability (i.e., inside the RMW), the situation is conducive to TC RI. Recent observational studies also proved this conclusion (Rogers et al., 2013). Yu and Yao (2011) pointed out that increased diabatic heating with height and enhanced vertical inhomogeneous heating near the TC inner core in the middle and upper troposphere are both favorable to TC RI. Therefore, it is scientifically necessary, particularly from a forecasting perspective, to further analyze the mechanism underlying the distribution and evolution of diabatic heating in the mid–upper troposphere with respect to the RI of offshore TCs.

With the development of high-resolution numerical modeling and our understanding of cloud microphysics, cloud-scale simulations of TCs have become one of the most effective and popular methods in this field of research. Cloud microphysics plays an important role in TC simulations (Zhu and Zhang, 2006). Different cloud microphysical parameterization schemes can ultimately affect the simulation of TC structure and intensity (Cecelski and Zhang, 2016). Developing more detailed and reasonable cloud microphysical schemes is important for better reflecting the distributions of water substances with different impacts on the structure of TC inner-core heating (McFarquhar et al., 2012). Comparing different cloud microphysical parameterization schemes, Ming et al. (2012) indicated that the condensation and depositional growth of graupel or snow in the Lin scheme (Chen and Sun, 2002) and Thompson scheme (Thompson et al., 2008) enhances the release of diabatic heat in the TC inner-core region. Li et al. (2013a, b) further showed that the total latent heat release during the entire life cycle of TC mainly comes from the latent heat of condensation in the middle and lower troposphere and the latent heat of deposition in the middle and upper troposphere. Furthermore, the significant latent heat of condensation for the development of TCs mainly comes from water vapor condensation into cloud water and depositional growth of cloud ice and snow. A recent study by Miller et al. (2015) showed that fusion latent heat had large positive impacts on the RI rate of Hurricane Wilma (2005). Furthermore, Li et al. (2019) pointed out that the deposition process in the upper level of the atmosphere was a critical factor for the convection bursts that triggered the RI onset of Super Typhoon Meranti (2016). Harnos and Nesbitt (2016) further confirmed the important role played by vertically developed deep convection and its associated ice processes within the RMW in the initiation and maintenance of RI. Although previous works have mostly been based on a limited number of TC samples or just one particular TC, they have nonetheless provided a good grounding of understanding with respect to RI from a microphysical-process perspective. As one TC varies from another, however, it is necessary to investigate different TC cases to form solid conclusions and gain a comprehensive understanding of the TC RI mechanism.

A recent RI TC case over the coastal waters of China, Hato (2017), is selected in this study, which is the strongest landfalling TC in the Pearl River Delta region since 1965. We focus on the microphysical latent heating budget during its RI process by quantitatively calculating and analyzing each latent heating-associated transformation rate in the cloud microphysical processes. More specifically, we investigate the mechanisms by employing latent-heating rates that are related to microphysical processes, as well as their relationship to RI, using a three-day, high-resolution (2-km) simulation of Typhoon Hato. Furthermore, each transformation rate and the associated latent heating term are calculated and outputted by modifying the default diagnostics field of the cloud microphysical scheme and the model. The TC inner-core cloud microphysical processes and the distribution characteristics of the corresponding latent heating are investigated. The next section provides an overview of the typhoon case. Section 3 describes the configuration of the model used in this study. Section 4 presents the simulation results as verified against various analyses and observations. Section 5 discusses the evolution of latent heat related to microphysical processes and its impact on the RI of Typhoon Hato. Section 6 presents the three-dimensional latent heat budget during the RI stage. Four ice phase-related microphysical-process sensitivity experiments are further designed and analyzed in Section 7, followed by summary and concluding remarks in Section 8.

2. Data and case overview

The best-track data of the Shanghai Typhoon Institute (Ying et al., 2014), China Meteorological Administration, along with ground-based weather radar data and

NCEP Final Operational Global Analysis (NCEP-FNL) data, at a spatial resolution of 0.25° × 0.25° and 3-h temporal resolution, are employed in this study. For the radar data, 20 individual radar observations around Guangzhou Station are used to generate the composite radar reflectivity.

Typhoon Hato formed as a tropical depression over the east of Luzon at 1800 UTC 19 August 2017, developing as the 13th named storm of that year and moving west-southwest, before further developing to become a tropical storm the next day. On 21 August, it passed over the northern portion of the South China Sea and reached typhoon intensity. It continued to intensify rapidly, and became a strong typhoon with a maximum wind speed of 52 m s^{-1} and central pressure of 935 hPa at 0300 UTC 23 August. Typhoon Hato underwent a 27-h intensification period, with a deepening rate of 27 m s^{-1} (50 hPa) from 0000 UTC 22 to 0300 UTC 23 August. In particular, from 0000 UTC to 0300 UTC 23 August, the maximum wind speed increased rapidly from 45 m s^{-1} to 52 m s^{-1}, with a minimum central pressure from 950 to 935 hPa. About 2 h later, at 0450 UTC 23 August, it made landfall at Zhuhai, Guangdong Province, with a maximum wind speed of 45 m s^{-1} and central pressure of 950 hPa. It further weakened over land and dissipated on 24 August in Yunnan Province of China. Hato was the strongest typhoon that landed in China in 2017, as well as the strongest landfalling typhoon in the Pearl River Delta region since 1965. Considering the characteristics of the evolution of Typhoon Hato intensity, as well as the commonly used RI criteria of a 15 m s^{-1} day^{-1} intensification of maximum wind (approximately 0.63 m s^{-1} h^{-1}), and for the convenience of description in the following analysis, the life history of Typhoon Hato is divided into three stages based on the intensification rate: the pre-RI stage (1800 UTC 21−1200 UTC 22) with an intensification rate of 0.56 m s^{-1} h^{-1}; the RI stage (1200 UTC 22−0300 UTC 23) with an intensification rate of 1.27 m s^{-1} h^{-1}; and the post-RI stage (0300 UTC 23−1800 UTC 23) with an intensification rate of −1.93 m s^{-1} h^{-1}. Detailed analysis of each stage and comparison among them will be given in later sections.

3. Model configuration

A 72-h simulation experiment is performed by using the Weather Research and Forecasting (WRF) model with the Advanced Research WRF (ARW) core (V3.8.1), referred to as WRF-ARW (V3.8.1), with a triple two-way interactive nested domain (18/6/2 km) grid. The simulation covers the development, RI, and subsequent landfall weakening stages of Typhoon Hato. All three domains (D01, D02, and D03) are integrated from 1800 UTC 21 August to 1800 UTC 24 August 2017; D02 and D03 are both automatic vortex-following moving nests, with the center of the domain located at the center of the typhoon (see Fig. 1).

The initial and boundary conditions are interpolated from the NCEP-FNL data, with a spatial resolution of 0.25° × 0.25° and 3-h temporal resolution. To enhance

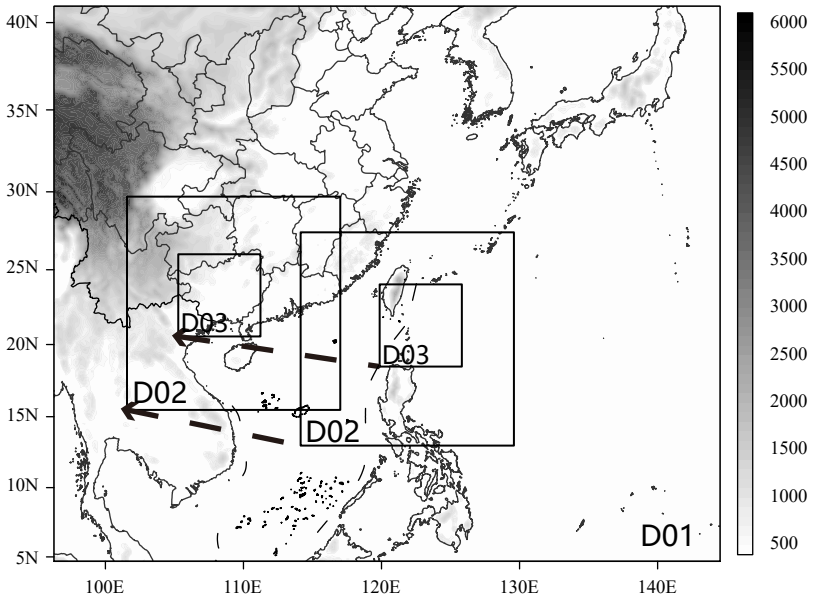

Fig. 1. The nested model meshes for domains D01, D02, and D03 with horizontal resolutions of 18, 6, and 2 km, respectively. The shadings represent the terrain height (m) greater than 500 m. The two dashed arrows indicate the moving direction of sub-domains D02 and D03.

the background TC vortex position, structure, and intensity, a dynamical vortex initialization scheme (Cha and Wang, 2013) with a topography-filtering algorithm (Liu et al., 2018a) is employed before the WRF integration. The model top is set at 10 hPa, and 55 sigma layers are used in the vertical direction. Considering the computation stability and universality to various weather systems, as well as some recent comparative study results showing that the single-moment 6-class (WSM6) microphysics parameterization scheme (Hong and Lim, 2006) performs better than other schemes in simulating RI (Lee and Wu, 2018; Qin et al., 2018; Pang et al., 2019), this scheme, which has been improved over its previous version (WSM5; Hong et al., 2004) by adding graupel-related processes (Lin et al., 1983; Rutledge and Hobbs, 1983, 1984), is used for all three domains. It contains six classes of water substance (i.e., water vapor, cloud water, cloud ice, graupel, rain, and snow). There are 36 types of cloud microphysical transformation processes, and 24 of them are associated with latent heating. Besides, the improved ice microphysics assumes the ice nuclei number concentration to be a function of temperature, and the ice crystal number concentrations to be a function of the amount of ice (Hong and Lim, 2006). The intercept parameter of snow particles is a function of temperature, and the freezing and melting processes are computed during the falling-term sub-steps to increase the computational accuracy of the heating profile in these processes. Like many other microphysics schemes, there are a vast number of assumptions or tunable parameters in the scheme. For interested readers, detailed descriptions of each sink/source term in the scheme can be found in the work of Hong and Lim (2006). The latent heating budgets associated with microphysical processes are calculated by using the 2-km simulation results and the model output with an interval of 1 h. The model configuration with regards to other physical processes is given in Table 1. Except for the cumulus parameterization scheme, which is not used in domain D03, the other physical parameterization schemes are used the same in all three domains (Table 1).

4. Model verification

In this section, we verify the 72-h model prediction of Typhoon Hato against various selected analyses and observations in order to demonstrate the simulation ability of the high-resolution WRF model in predicting the track, intensity, and inner-core structures of Typhoon Hato.

4.1 *Track and intensity*

For a comprehensive verification, we firstly compare the model-simulated track of Hato to the best-track data analysis (Fig. 2). It is clear that the model reproduces the northwestward movement generally well; also, the propagation speed is close to the best-track analysis. The location of the landfall is about 35 km east of the actual

Table 1. Model configuration for the control experiment

Domain	D01	D02	D03
Horizontal grid number	311 × 251	271 × 271	313 × 313
Grid spacing (km)	18	6	2
Integration time (h)	72	72	72
Cumulus parameterization	Kain–Fritsch (Kain, 2004)		Not used
Microphysics	Single-moment 6-class (Hong and Lim, 2006)		
Planetary boundary layer	Yonsei University scheme (Hong et al., 2006)		
Radiation Scheme	Rapid and Accurate Radiative Transfer Model (Iacono et al., 2008)		

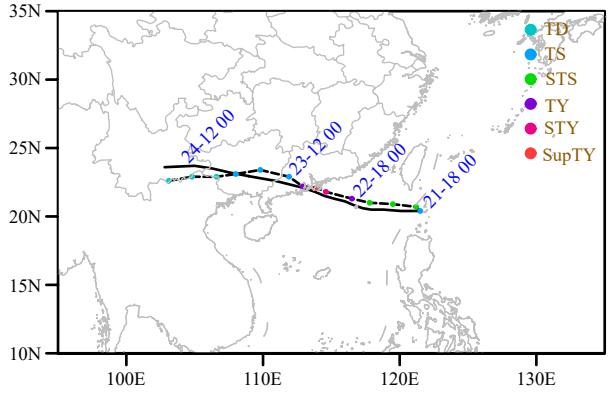

Fig. 2. Comparison of the simulated storm track (dashed line) and the best-track data (solid line) of Typhoon Hato during 1800 UTC 21−1800 UTC 24 August 2017.

situation.

The temporal evolution of the predicted typhoon intensity in terms of minimum sea level pressure and maximum surface wind speed are compared to the best track in Fig. 3. Compared with the numerical simulation results and the best track, although there are differences in the specific values at each specific moment, the trends of the two changes are very consistent; i.e., the initial spin up, followed by an RI stage, and the subsequent weakening and dissipation stage. The simulated maximum surface wind speed is 54.3 m s^{-1}, which is larger than in the best-track data (52 m s^{-1}), but they both appear at the same time of 0300 UTC 23 August 2017.

4.2 *Radar reflectivity*

Figure 4 compares the maximum radar reflectivity structure and its evolution in the model-simulated results with real-time radar observations during the RI stage of Hato. Overall, the model results reflect the TC eye, inner-core asymmetric eyewall, and outer spiral rainband pattern. More specifically, due to the limited coverage of radar, there are no observational data available to be compared with in the southeast quadrant of typhoons south of 20°N (Figs. 4a, c, e), but the model results show a prominent peripheral spiral rainband (Figs. 4b, d). In addition, this rainband can be captured by real-time satellite images (figure omitted). Focusing on the inner core, the model reproduces the asymmetric structures of the intense spiral rainbands, eyewall, and echo-free eye. Note that the simulated eyewall in the southwest quadrant shows strong convection, which is slightly wider than that observed. The same deficiency has been reflected in simulations of Hurricane Andrew (Liu et al., 1997) and Patricia (Qin et al., 2018). Because of the discrepancy in resolution between the radar and model, the differences are acceptable in the following analysis. Besides, the distribution pattern of the rain belt simulated by the model is consistent with the observation, but the model generally overestimates the precipitation along the TC track (figure omitted).

5. Intensity change and associated latent heating

Figure 5 shows the azimuthal and time-averaged hydrometeors (water vapor, rainwater, cloud water, cloud ice, snow, and graupel) of the 456 km × 456 km domain around the inner core in the pre-RI, RI, and post-RI stages of Typhoon Hato. Similarly, the averaged potential temperature perturbation, tangential wind, vertical velocity, and the secondary circulation during the pre-RI, RI, and post-RI stages of Typhoon Hato are further illustrated in Fig. 6. The change characteristics of water substances in these three stages of Hato and their relationship with the structural characteristics of the inner-core region are analyzed in the following passage.

During the three stages of Hato as mentioned above, the inner-core region of the typhoon has abundant water vapor supply, and the water vapor content changes little. The water vapor distribution is relatively uniform both in the horizontal and vertical direction; the radial gradient is close to zero, and little variation exists inside and outside the eyewall (Fig. 5). Overall, the vertical gradient changes little before and after the RI process. Compared with the other five water substances, the water vapor content changes minimally before and after the RI process, which is related to the typhoon's activity over the ocean during this period and strong inflow in the boundary layer (Fig. 6), thus possessing a continuous supply of water vapor. It should be pointed out that our simulation

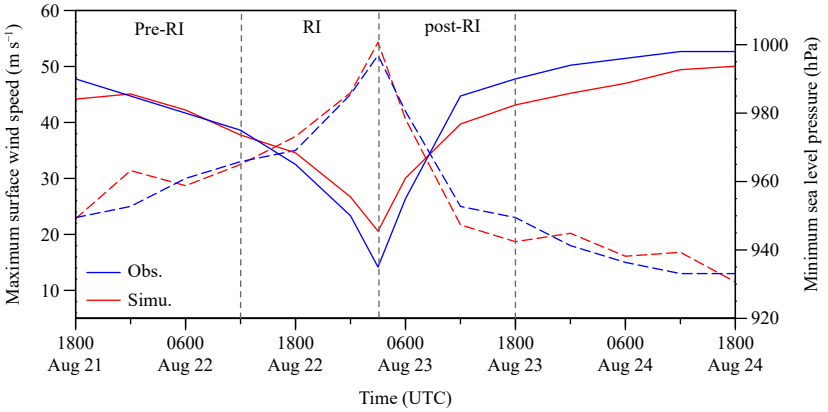

Fig. 3. Time series of the simulated (Simu; red) and best-track (Obs; blue) maximum surface wind speed (dashed line; m s^{-1}) and minimum sea level pressure (solid line; hPa) of Typhoon Hato during 1800 UTC 21−1800 UTC 24 August 2017. The pre-RI (1800 UTC 21−1200 UTC 22), RI (1200 UTC 22−0300 UTC 23), and post-RI (0300 UTC 23−1800 UTC 23) periods are separated by three vertical gray dashed lines.

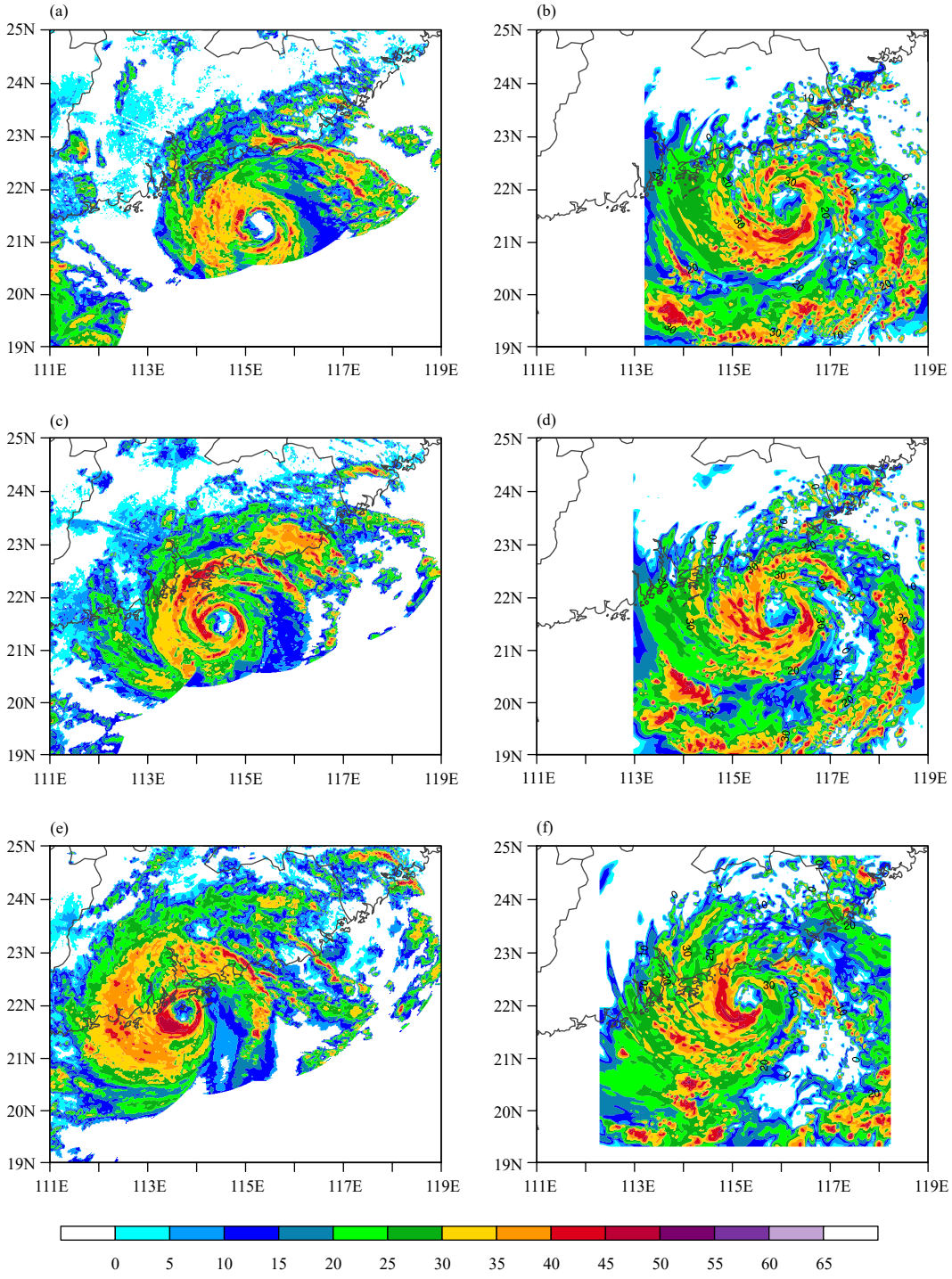

Fig. 4. Horizontal maps of the (a, c, e) observed and (b, d, f) simulated composite radar reflectivity (shading; dBZ) valid at (a, b) 2100 UTC 22, (c, d) 0000 UTC 23, and (e, f) 0300 UTC 23 August 2017, respectively.

results might be improved further by using an atmosphere–ocean-wave coupled model, since the SST cooling effect (Bender et al., 1993), subsurface ocean anomaly (Lin et al., 2009), and sea spray (Ma et al., 2017) can be fully taken into consideration under high-wind conditions.

For the two types of liquid water substances: rainwater and cloud water, in the pre-RI phase, they are mainly concentrated in the typhoon eyewall area below 6 km, and there also exists a small amount in the rainband outside the typhoon center 200 km away. In the RI phase, both the rainwater and the cloud water in the eyewall in-

crease, and the maximum belts are respectively below 2–4 and 2 km. Besides, the large-value area extends beyond the eyewall (Fig. 5d), and this corresponds to the enhanced upward motion in the eyewall region (Fig. 6b). In

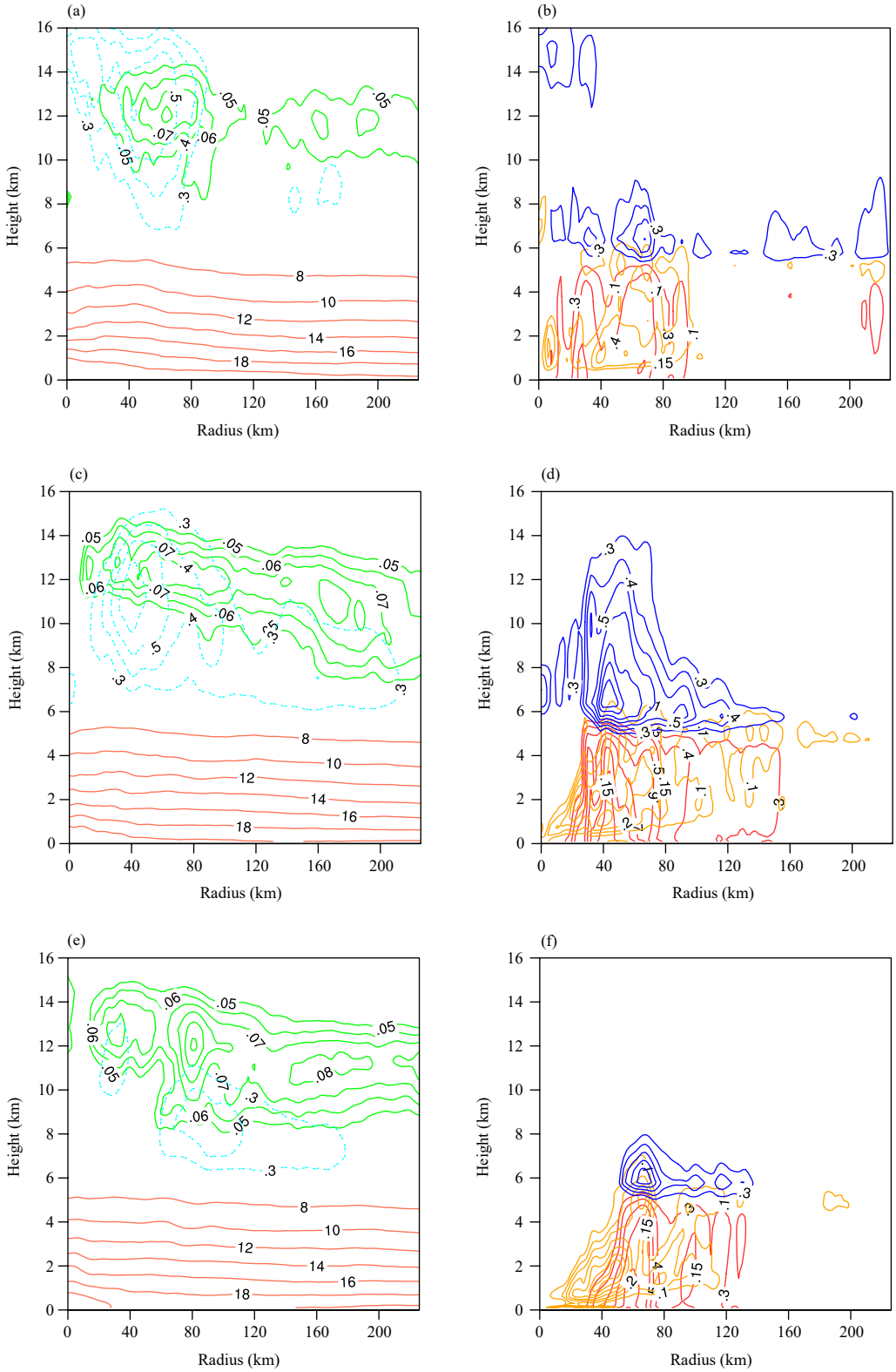

Fig. 5. Azimuthal- and time-averaged mixing ratio (contours; g kg^{-1}) of six hydrometeors in WSM6: (a, c, e) water vapor (coral line), cloud ice (green line), and snow (cyan line); (b, d, f) rainwater (gold line), cloud water (red line), and graupel (blue line) during the (a, b) pre-RI, (c, d) RI, and (e, f) post-RI stages of Typhoon Hato.

the post-RI phase, as the intensity of the typhoon weakens, the vertical velocity in the eyewall also weakens (Fig. 6c), and the rainwater and cloud water decrease significantly.

For the three types of solid water substances (ice, snow, and graupel) in the pre-RI stage, graupel is mainly distributed in the middle layer of the troposphere at 6–8 km, and spreads to the entire typhoon inner-core area. Cloud ice is mainly distributed in the upper troposphere at 10–14 km, with a large radial gradient. Snow is mainly distributed in the upper troposphere above 10 km from the center of the typhoon to the eyewall. In the RI stage, the graupel located in the eyewall of the middle troposphere increases rapidly with obviously vertical upward transport (Fig. 6b), but decreases outside the eyewall. At the same time, the cloud ice and snow in the entire inner core increase. Again, there is clear vertical upward development in the eyewall region. In the post-RI stage, graupel and snow reduce significantly. The distribution pattern of cloud ice changes little, and the radius of the eyewall becomes larger, corresponding to the cloud ice maximum value center moving along the outflow direction. Overall, in the RI stage, there is a significant increase for the three types of solid water substances (ice, snow, and graupel) at 8–12 km in the middle and upper troposphere of the eyewall of Hato, which corresponds to the enhanced TC secondary circulation, and this process is accompanied by the formation of the upper-level warm core and enhancement of the lower-level warm core (Fig. 6b), which is consistent with findings reported for the RI of Hurricane Wilma (Miller et al., 2015; Qin et al., 2018).

Equations (1)–(6) below are used to calculate the latent heating of microphysical processes. Here, Q_{con} is the net latent heat rate (K h^{-1}) associated with the process of condensation, Q_{evp} with evaporation, Q_{frz} with freezing, Q_{mlt} with melting, Q_{dep} with deposition, and Q_{sub} with sublimation. L_v, L_f, and L_s are the latent heat of condensation, fusion, and sublimation, respectively, which are functions of temperature T, when T_0 = 273.15 K, L_v = 2.50 × 10^6 J kg^{-1}, L_f = 0.35 × 10^6 J kg^{-1}, and L_s = 2.85 × 10^6 J kg^{-1}, in the calculation process of the WSM6 scheme. C_{pm} is the specific heat of moist air at constant pressure: $C_{pm} = C_{pd} \times (1 - q) + q \times C_{pv}$, where C_{pd} = 1005.7 J kg^{-1} K^{-1}, C_{pv} = 1870 J kg^{-1} K^{-1}, and q is the mixing ratio of water vapor. P_{xxxx} is the production rate (kg kg^{-1} s^{-1}) of each microphysical process, and the specific meaning of each term is listed in Table 2.

$$Q_{con} = L_v \times P_{cond}/C_{pm}, \tag{1}$$

$$Q_{evp} = L_v \times \left(P_{evap} + P_{revp} + P_{sevp} + P_{gevp}\right)/C_{pm}, \tag{2}$$

$$Q_{frz} = L_f \times (P_{ihmf} + P_{ihtf} + P_{gfrz} + P_{iacr} + P_{gacr} + P_{sacr} + 2 \times P_{aacw})/C_{pm}, \tag{3}$$

$$Q_{mlt} = L_f \times \left(P_{smlt} + P_{gmlt} + P_{imlt} + P_{seml} + P_{geml}\right)/C_{pm}, \tag{4}$$

$$Q_{dep} = L_s \times \left(P_{idep} + P_{sdep} + P_{gdep} + P_{igen}\right)/C_{pm}, \tag{5}$$

$$Q_{sub} = L_s \times \left(P_{isub} + P_{ssub} + P_{gsub}\right)/C_{pm}, \tag{6}$$

$$Q_{total} = Q_{con} + Q_{evp} + Q_{frz} + Q_{mlt} + Q_{dep} + Q_{sub}. \tag{7}$$

Latent heating is the main energy source for the development of a TC, playing a leading role in TC intensity

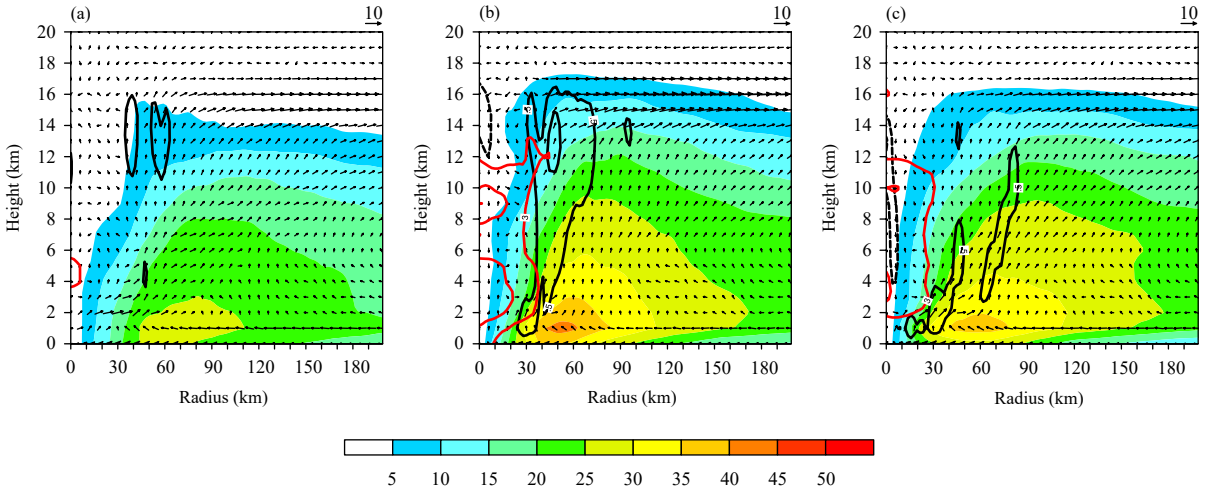

Fig. 6. Azimuthally and temporally averaged potential temperature perturbation (red contours; K), tangential wind (shading; m s^{-1}), vertical velocity (black contours; m s^{-1}), and the secondary circulation (arrows; m s^{-1}) during the (a) pre-RI, (b) RI, and (c) post-RI stages of Typhoon Hato.

Table 2. Average vertical integration of the microphysical latent heat rate budget and its standard deviation of the inner-core region during the RI stage of Typhoon Hato

Production rate	Microphysical process	Latent heat rate (K h^{-1})	Percentage (%)
P_{cond}	Condensation of cloud water	35.78 ± 1.91	67.59% ± 3.60%
P_{idep}	Deposition of ice	6.83 ± 0.37	12.90% ± 0.70%
P_{igen}	Generation (nucleation) of ice from vapor	4.18 ± 0.27	7.90% ± 0.51%
P_{sdep}	Deposition of snow	3.52 ± 0.23	6.65% ± 0.43%
P_{gdep}	Deposition of graupel	1.12 ± 0.09	2.12% ± 0.02%
P_{aacw}	Accretion of cloud water by snow and graupel	1.06 ± 0.09	2.00% ± 0.02%
P_{gacr}	Accretion of rain by graupel	0.18 ± 0.00	0.34% ± 0.00%
P_{iacr}	Accretion of rain by cloud ice	0.15 ± 0.00	0.28% ± 0.00%
P_{sacr}	Accretion of rain by snow	0.08 ± 0.00	0.15% ± 0.00%
P_{ihmf}	Homogeneous freezing of cloud water to form cloud ice	0.04 ± 0.00	0.08% ± 0.00%
P_{gfrz}	Freezing of rainwater to graupel	0.00 ± 0.00	0.00% ± 0.00%
P_{ihtf}	Heterogeneous freezing of cloud water to form cloud ice	0.00 ± 0.00	0.00% ± 0.00%
	Total heating	**52.94**	**100%**
P_{revp}	Evaporation of rain	−6.66 ± 0.31	47.57% ± 2.21%
P_{smlt}	Melting of snow to form cloud water	−3.88 ± 0.14	27.71% ± 1.00%
P_{gmlt}	Melting of graupel to form cloud water	−1.37 ± 0.06	9.79% ± 0.42%
P_{gevp}	Evaporation of melting graupel	−0.59 ± 0.04	4.21% ± 0.28%
P_{geml}	Induced by enhanced melting rate of graupel	−0.44 ± 0.02	3.14% ± 0.14%
P_{ssub}	Sublimation of snow	−0.38 ± 0.02	2.71% ± 0.14%
P_{evap}	Evaporation of cloud water into water vapor	−0.20 ± 0.01	1.43% ± 0.07%
P_{sevp}	Evaporation of melting snow	−0.19 ± 0.00	1.36% ± 0.00%
P_{gsub}	Sublimation of graupel	−0.19 ± 0.00	1.36% ± 0.00%
P_{isub}	Sublimation of cloud ice	−0.07 ± 0.00	0.50% ± 0.00%
P_{seml}	Induced by enhanced melting of snow	−0.02 ± 0.00	0.14% ± 0.00%
P_{imlt}	Instantaneous melting of cloud ice	−0.01 ± 0.00	0.07% ± 0.00%
	Total cooling	**−14.00**	**100%**
	Net microphysical latent heat	**38.94**	

change (Malkus and Riehl, 1960; Anthes, 1982; Nolan and Grasso, 2003; Nolan et al., 2007). The evolutionary characteristics of water substances before and after RI are analyzed. The vertical profile of the microphysical latent heating rate (Fig. 7) is calculated during the pre-RI, RI, and post-RI stages of Typhoon Hato, with equal time intervals.

Consistent with the evolutionary characteristics of the warm core (Fig. 6), the results show that the total microphysical latent heating rate of the inner-core region reaches a maximum in the RI stage at 2100 UTC 22 August 2017, contrasting with the pre- and post-RI stages (Fig. 7). The total latent heating is mainly characterized by a significant increase in the middle to upper troposphere (5–12 km). In the surface layer, below 0.5 km, negative latent heating is continuously maintained, due to the effect of evaporative cooling, but it is slightly less in the RI stage than in the pre- or post-RI stage. From 0.5 to 6 km, the total microphysical latent heating is mainly contributed by condensation heating and melting cooling, and reaches its maximum and minimum at 5 km. At this height, due to the remarkable melting cooling, the total heating profile shows an inversion pattern. Similarly, the condensation heating reaches its maximum at this height, which clearly compensates the melting cooling effect. Above 6 km, the condensation heating decreases rapidly with height. Meanwhile, deposition heating increases, and gradually becomes the major positive contributor to the total microphysical latent heating, while the melting cooling decreases with height.

Overall, in the RI stage of Typhoon Hato, the total latent heating shows a significant increase with height from 0.5 to 15 km. At a height of 5 km, the net freezing heating and melting cooling reaches its maximum, and the condensation heating is partly balanced by the melting cooling. Above 6 km, the net deposition heating begins to increase and, from 8 km and above, the deposition heating becomes the major contributor to the total latent heating in the atmospheric column, coupled with the reduced condensation heating, resulting in the total latent heating reaching a maximum at 9 km. This indicates that, in the middle to upper troposphere (6–15 km), due to the enhanced upward motion in the eyewall region (Fig. 6b), more kinds of water substances corresponding to more complicated cloud microphysical processes play different roles at different heights. Thus, coupled together, they greatly impact the structure and change in intensity of the typhoon, particularly in the RI stage. It is worth

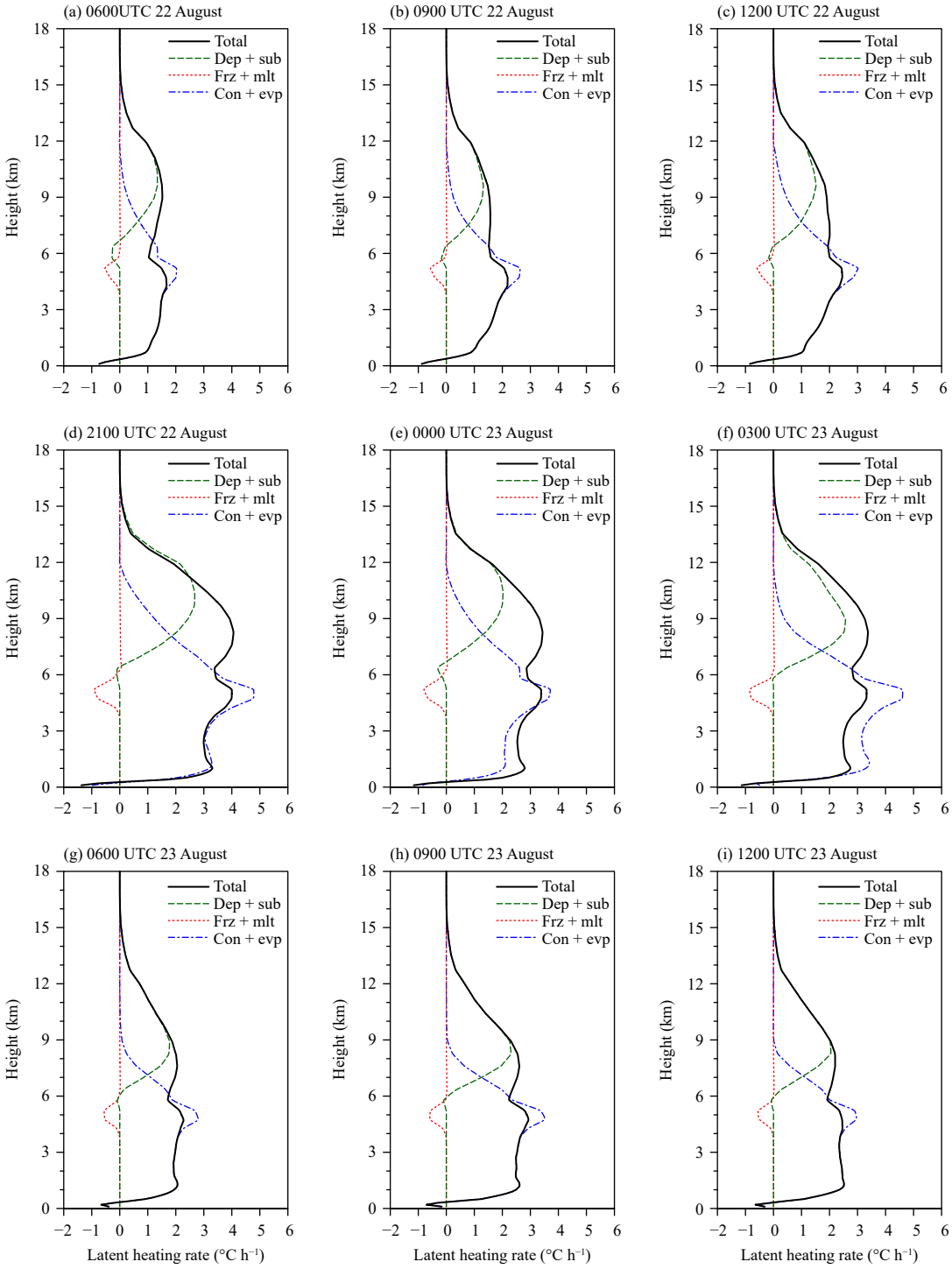

Fig. 7. Vertical profiles of the microphysical latent heating rate (°C h^{-1}) during (a–c) the pre-RI, (d–f) RI, and (g–i) post-RI stages of Typhoon Hato for the total latent heating profile (black solid line), condensation- and evaporation-associated heating (blue dotted-dashed line; con + evp), freezing- and melting-associated heating (red dotted line; frz + mlt), and deposition- and sublimation-associated heating (green dashed line; dep + sub).

noting that convective cells possess considerable randomness and uncertainty in typhoon circulation. The focus of this study is the thermodynamic budget of the azimuthal and temporal average of the whole inner-core region of Hato, i.e., not specific to each convective cell.

6. RI and microphysical latent heating budget

To further understand the three-dimensional structure of the microphysical latent heating rate during the RI

stage of Typhoon Hato, Fig. 8 shows the radius–height vertical distributions of three kinds of latent heating: condensation- and evaporation-associated latent heating; freezing- and melting-associated latent heating; and deposition- and sublimation-associated latent heating; as well as the total.

The large-value center of the condensation heating of water vapor is mainly distributed in the eyewall area below the 0°C isotherm layer, at about 3–6 km (Fig. 8a, solid line). In the boundary layer near the ocean surface, the latent heating is dominated by evaporative cooling (Fig. 8a, dashed line). Freezing heating is mainly distributed above the 0°C isotherm layer, which is also mainly located in the eyewall, but its contribution to the total latent heating is limited. Melting cooling is mainly distributed below the 0°C isotherm layer, which also reaches its maximum in the eyewall region and is distributed throughout the inner-core region (Fig. 8b). Deposition heating is mainly located at 8–14 km, reaching a maximum at 11 km in the eyewall region. Around the eye of the typhoon, sublimation cooling exists, which is related to the warm downdraft in the typhoon eye (Fig. 8c).

In general, in the air–sea boundary layer and near the ocean surface, microphysical latent heating is dominated by water vapor evaporative cooling (Fig. 8d). In the lower troposphere (0–4 km), water vapor condensation heating is the dominant process, while the upper troposphere (above 10 km) is dominated by deposition heating. The heating composition in the middle layer of the troposphere (4–10 km) is relatively complicated, with condensation heating (Fig. 8a), freezing heating (Fig. 8b), and deposition heating (Fig. 8c) existing simultan-

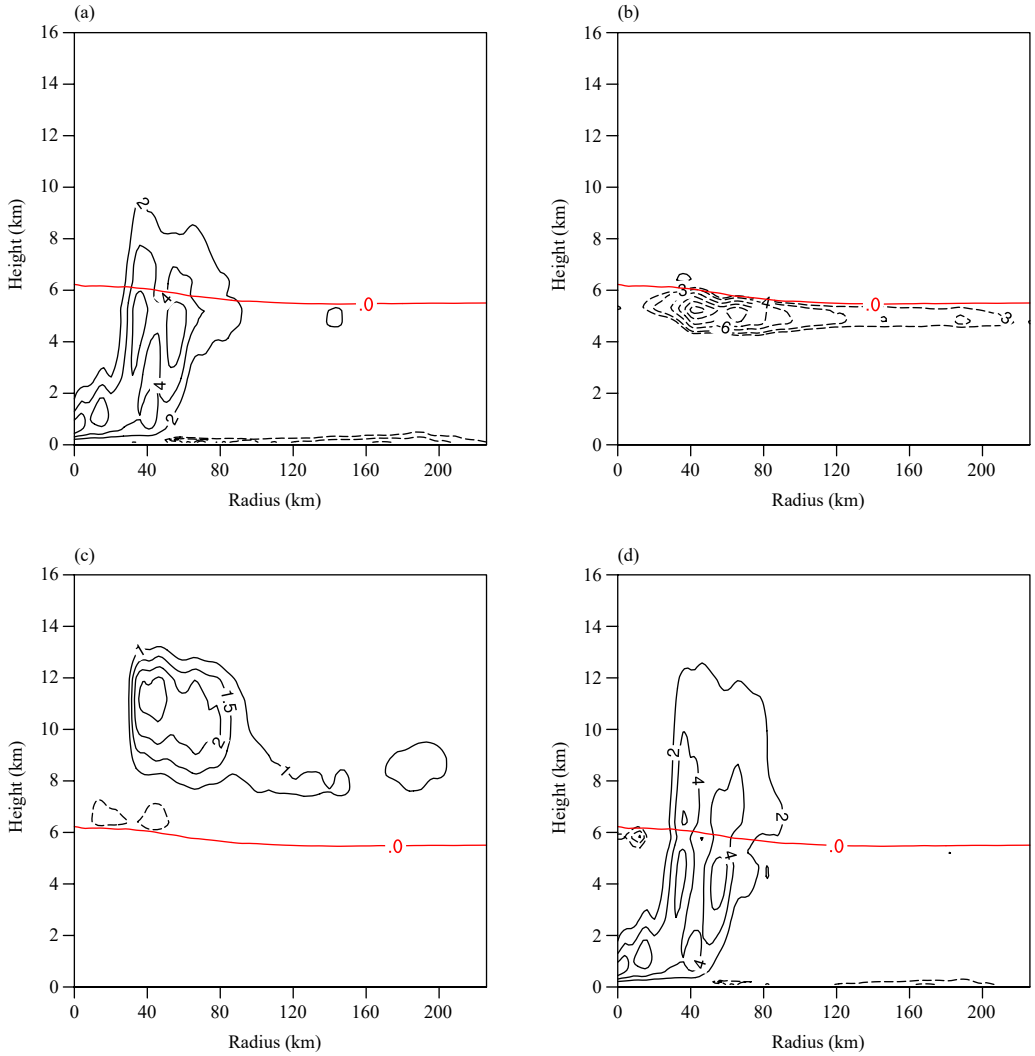

Fig. 8. Azimuthally and temporally averaged microphysical latent heating rate (contours; °C h^{-1}) in the RI stage of Typhoon Hato for (a) condensation/evaporation process (solid/dashed lines); (b) freezing/melting process (solid/dashed lines); (c) deposition/sublimation process (solid/dashed lines); and (d) the total microphysical process. Red solid line represents the 0°C isotherm.

eously. Besides, sublimation cooling and melting cooling exist simultaneously; thus, coupled together, these components present the total latent heating structure and evolutionary pattern, which is closely associated with the RI of Hato (Fig. 8c).

To further understand the vertical structure of latent heating, especially the relatively complicated cloud microphysical activity and the associated heat release and absorption of heat in the middle troposphere, and to explore the relative importance of each cloud microphysical process to the latent heating budget, Table 2 illustrates the vertical integration of the microphysical latent heat budget of the inner-core region of Typhoon Hato during the RI stage, which involves all 24 types of cloud microphysical processes accompanied by latent heat changes in the WSM6 scheme.

From a column vertical integration viewpoint, the rate of latent heat release associated with the condensation of cloud water can reach 35.78 K h^{-1}, accounting for 67.59% of the total latent heat (Table 2). This is followed by the deposition rate of ice, the generation (nucleation) of ice from vapor, and the deposition rate for snow, accounting for 12.9%, 7.9%, and 6.65% of the total latent heating, respectively. The latent heat released by the above four microphysical processes accounts for more than 95% of the total latent heat. On the other hand, the top five latent heat cooling processes are the evaporation of rain, the melting of snow to form cloud water, the melting of graupel to form cloud water, the evaporation of melting graupel, and the enhanced melting rate of graupel, accounting for 47.57%, 27.71%, 9.79%, 4.21%, and 3.14% of the total latent cooling, respectively. The latent heat absorbed by the above five microphysical processes accounts for more than 90% of the total latent cooling. It can be concluded that the microphysical processes that play a leading role in the evolution of total latent heat are these nine microphysical processes mentioned above (Table 2). Taking the standard deviation into account, the top four microphysical processes with positive latent heating (heating effect) contribution can still maintain the larger contribution, but the latent heat contribution of the other microphysical processes will vary. To further understand the evolution of the latent heat released and absorbed in association with the above major cloud microphysical processes, the top four most important microphysical processes associated with the release and absorption of latent heat in the RI stage of Typhoon Hato are shown in Figs. 9, 10.

As shown in Fig. 9, the condensation of water vapor into cloud water occurs almost throughout the troposphere in the vertical direction, reaches a maximum at 5 km in the typhoon eyewall region, and reduces with the radius away from the TC eyewall. It is worth noting that there is also a condensation heating zone below 2 km in the eye of Typhoon Hato, which is related to the low-level cloud activity in the typhoon eye. The latent heat due to the deposition rate of ice is mainly distributed around 10 km near the −15°C isotherm, as is the generation (nucleation) of ice from vapor, while the deposition rate for snow is located around 11 km. The above four main latent heating processes occur in the middle and upper troposphere. This suggests that, when RI occurs in a TC, special attention should be paid to the diabatic heating evolution of the TC eyewall region in the middle troposphere. The importance of water vapor condensation heating has reached a consensus, with several related studies drawing similar conclusions. For example, Li et al. (2013a) demonstrated that the water vapor condensation heating accounts for 73.2% of the total microphysical heating for Typhoon Hagupit (2008). Li et al. (2019) pointed that the condensation of water vapor accounts for 76.3% of the total heating for Typhoon Meranti (2016). Taking the latest research (Tang et al., 2018, 2019; Li et al., 2019) into account, we should pay special attention to the cloud ice and snow deposition and generation (nucleation) processes in the upper troposphere and their accompanying latent heating.

As shown in Fig. 10, first and foremost, the evaporation of rain is the most important latent cooling item. Its contribution to the total latent cooling rate is close to half, and the stronger cooling occurs in the lower troposphere between 2 and 4 km. Unlike condensation heating, the radial gradient of the process is relatively small; that is, there always exists a cooling effect of the evaporation of rain in the lower troposphere of the TC inner-core region. Second, the latent cooling associated with the melting of snow to form cloud water mainly occurs in the shallow layer below the 0°C isotherm layer, at about 5–6 km. Its radial distribution is relatively uniform and the gradient is small, but its absolute value is large and contributes greatly to the total cooling, followed by the melting of graupel to form cloud water and evaporation of melting graupel distributed below the 0°C isotherm layer in the eyewall region. In conclusion, the above four main latent cooling processes occur in the middle and lower troposphere, and special attention needs to be paid to the latent cooling between 5 and 6 km in a predictive sense, which causes the total latent heat profile to decrease at this height, similar to the "inverse temperature"

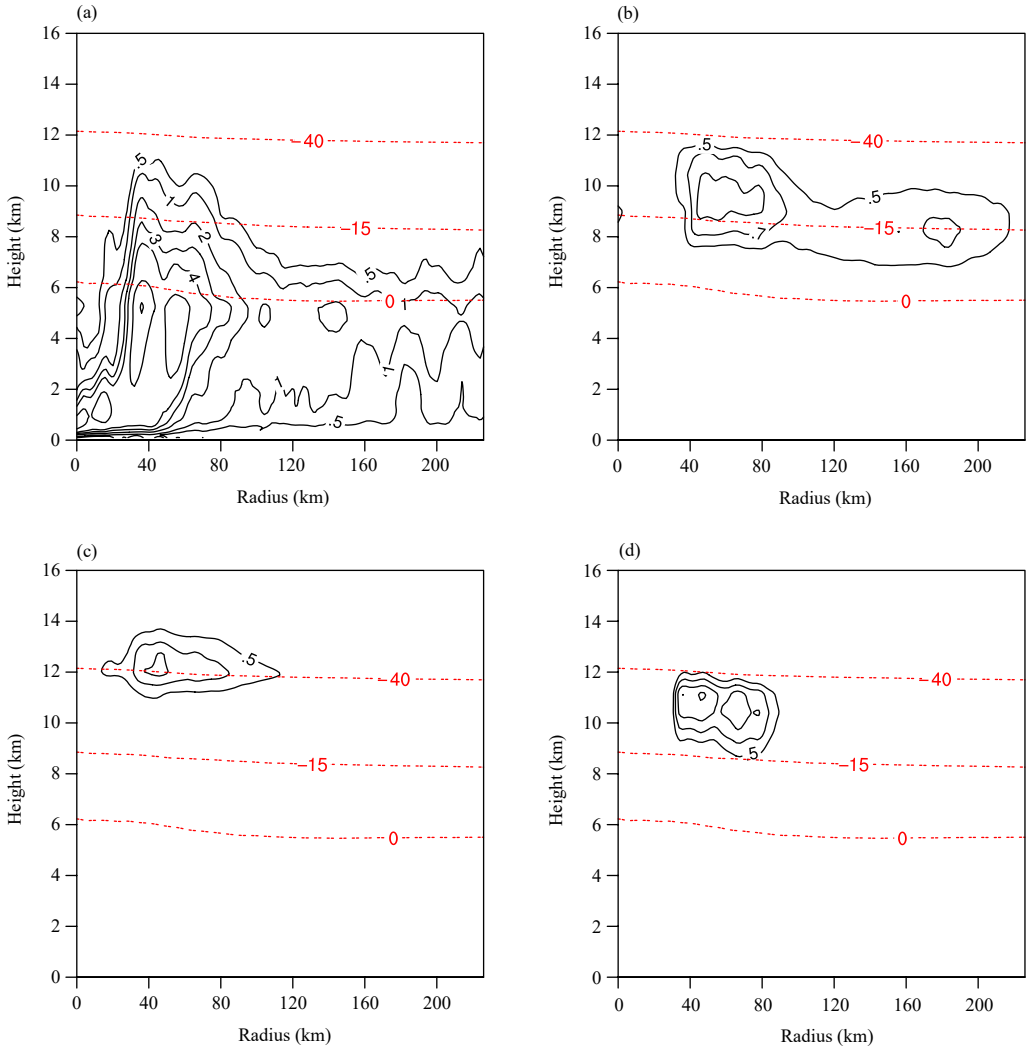

Fig. 9. Production rate (contours; kg kg^{-1} s^{-1}) for top four most important positive microphysical processes in the RI stage of Typhoon Hato: (a) condensation of water vapor into cloud water; (b) deposition of ice; (c) generation (nucleation) of ice from vapor; and (d) deposition of snow. The red dashed lines indicate the 0, −15, and −40°C isotherms.

profile pattern (see Fig. 7 for details).

For a more detailed and intuitive expression, following Table 2, combined with the schematic diagram of the cloud microphysical conversion processes of water substances in the WSM6 scheme, Fig. 11 shows the time-averaged vertical integration of the microphysical latent heat budget of Typhoon Hato during the RI stage, which includes all 24 types of cloud microphysical processes associated with latent heat changes in the WSM6 scheme. Considering the relative contributions of the various microphysical processes to the latent heat budget revealed that the main positive microphysical processes for the RI of Typhoon Hato are water vapor condensing into cloud water, the deposition rate of ice, generation (nucleation) of ice from vapor, and the deposition rate for snow. Meanwhile, the main negative microphysical processes to RI of Typhoon Hato are the evaporation of rain, the melting of snow to form cloud water, the melting of graupel to form cloud water, the evaporation of melting graupel, and the enhanced melting rate of graupel. The latent heating/cooling associated with other physical processes is shown in detail in Fig. 11.

7. Sensitivity experiments

Four ice phase-related microphysical process sensitivity experiments are designed to explore the main conclusions drawn from the control simulation. Detailed descriptions of each sensitivity experiment are provided in Table 3.

The maximum surface winds of the four sensitivity experiments are compared with that of the control experi-

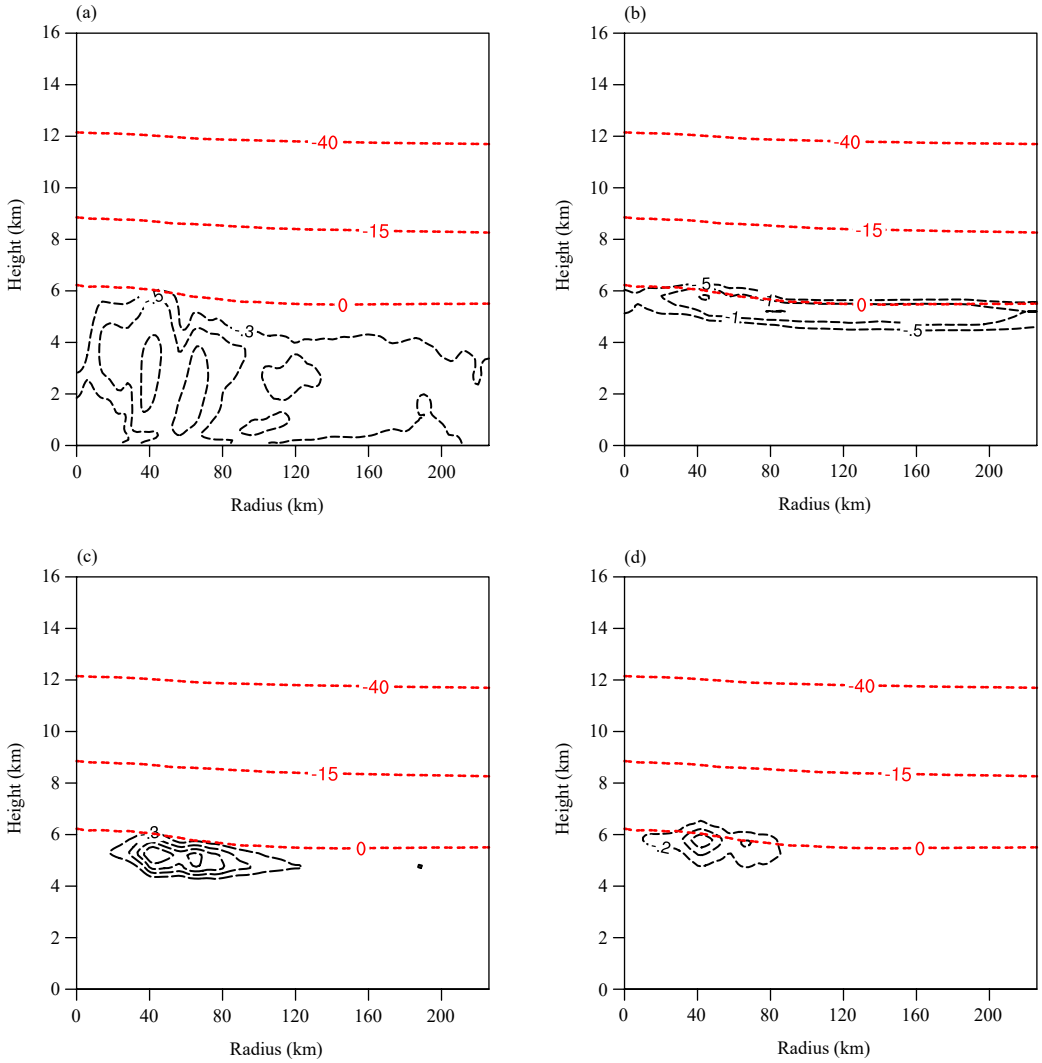

Fig. 10. Production rate (contours; kg kg^{-1} s^{-1}) for four most important negative microphysical processes in the RI stage of Typhoon Hato: (a) evaporation of rain; (b) melting of snow to form cloud water; (c) melting of graupel to form cloud water; and (d) evaporation of melting graupel. The red dashed lines indicate the 0°C, −15°C, and −40°C isotherms.

ment and the best analysis in Fig. 12. The results show that the intensification speed and the ultimate peak intensity are highly correlated with these four microphysical processes.

Specifically, in the NoSMLT experiment, Hato shows the highest RI rate from 1200 UTC 22 to 1800 UTC 22 August 2017, as well as the strongest peak intensity, which is followed by the NoGMLT experiment. On the contrary, in the NoIDEP experiment, Hato shows the weakest peak intensity and even quickly weakens at 1800 UTC 22 August 2017. The same variations are also shown in the NoIDEP experiment. We can conclude that the microphysical latent heating from the depositional growth of ice and the generation (nucleation) of ice contributes greatly to the RI of Hato and the microphysical latent cooling from the melting of snow and the graupel to form cloud water slows down the intensification speed and the ultimate peak intensity to some extent.

Table 3. Summary of the ice phase–related microphysical process sensitivity experiments

Experiment	Description
CTL	Control simulation with the WSM6 microphysical scheme
NoGMLT	As in CTL but without the latent cooling of melting of graupel to form cloud water
NoSMLT	As in CTL but without the latent cooling of melting of snow to form cloud water
NoIGEN	As in CTL but without the latent heating of the nucleation of ice from vapor
NoIDEP	As in CTL but without the latent heating of depositional growth of ice

The differences of each sensitivity test are analyzed in terms of the convection and mass flux by combining the characteristics of inflow in the boundary layer and outflow in the upper layer associated with the secondary cir-

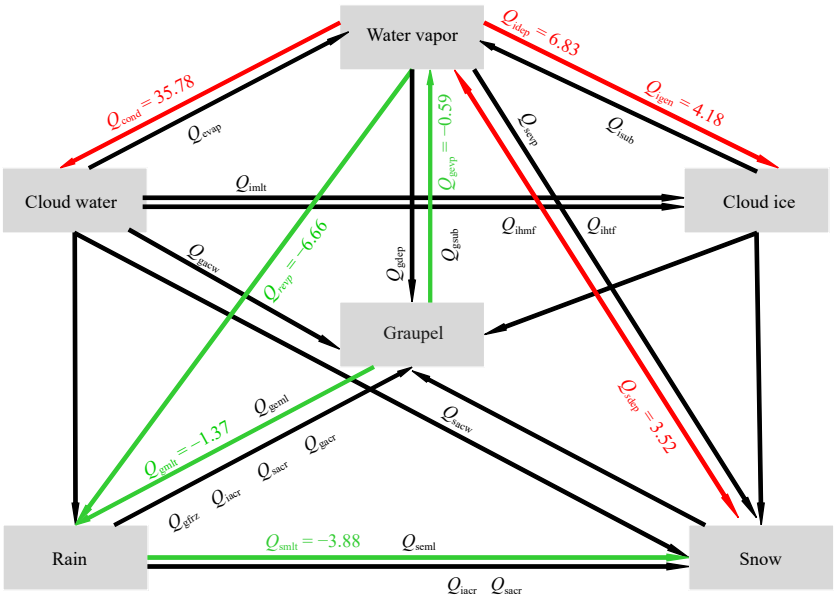

Fig. 11. Microphysical processes and their associated latent heat rate budget (Q; K h^{-1}) in the WSM6 scheme during the RI stage of Typhoon Hato. Red arrows indicate the top four most important microphysical processes associated with net heating. Green arrows indicate the top four most important microphysical processes associated with net cooling. The other latent heat rate values of microphysical processes are omitted and indicated by black arrows.

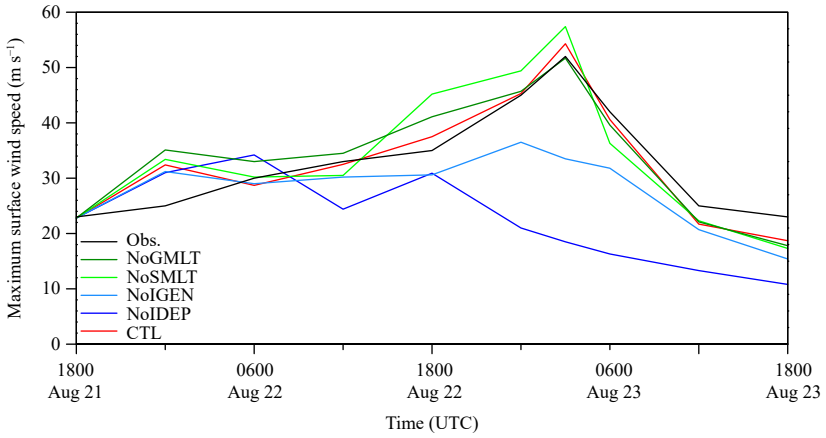

Fig. 12. Time series of the maximum surface wind speed (m s^{-1}) from the best analysis (Obs.; black line), control simulation (CTL; red line), and four ice-phase microphysical process sensitivity experiments (green/ blue lines).

culation. Figure 13 compares the azimuthally and temporally averaged mass flux and convection characteristics of the control simulation and two of the sensitivity experiments: NoSMLT and NoIDEP.

Compared with the control simulation (Figs. 13a, b), the simulated Hato shows the strongest secondary circulation and minimum RMW in the NoSMLT experiment, which are characterized by the stronger vertical mass flux in the eyewall region (Fig. 13c) and larger reflectivity in the boundary layer within the RMW (Fig. 13d). This indicates that the cooling effect of the melting of snow to form cloud water can restrain the speed of RI and the ultimate peak intensity of the simulated Hato to some extent. For the NoIDEP experiment, the simulated Hato shows the weakest secondary circulation and reflectivity among all the sensitivity experiments, which corresponds to its intensity change (Fig. 12). One striking feature is that the convective activity in the upper troposphere near 10 km (Fig. 13f) is obviously weakened in terms of its range and intensity compared with the control experiment results (Fig. 13b). Besides, the convective activity in the lower troposphere below 4 km is mainly located outside the RMW, and the related vertical mass flux (Fig. 13e) is significantly reduced. This

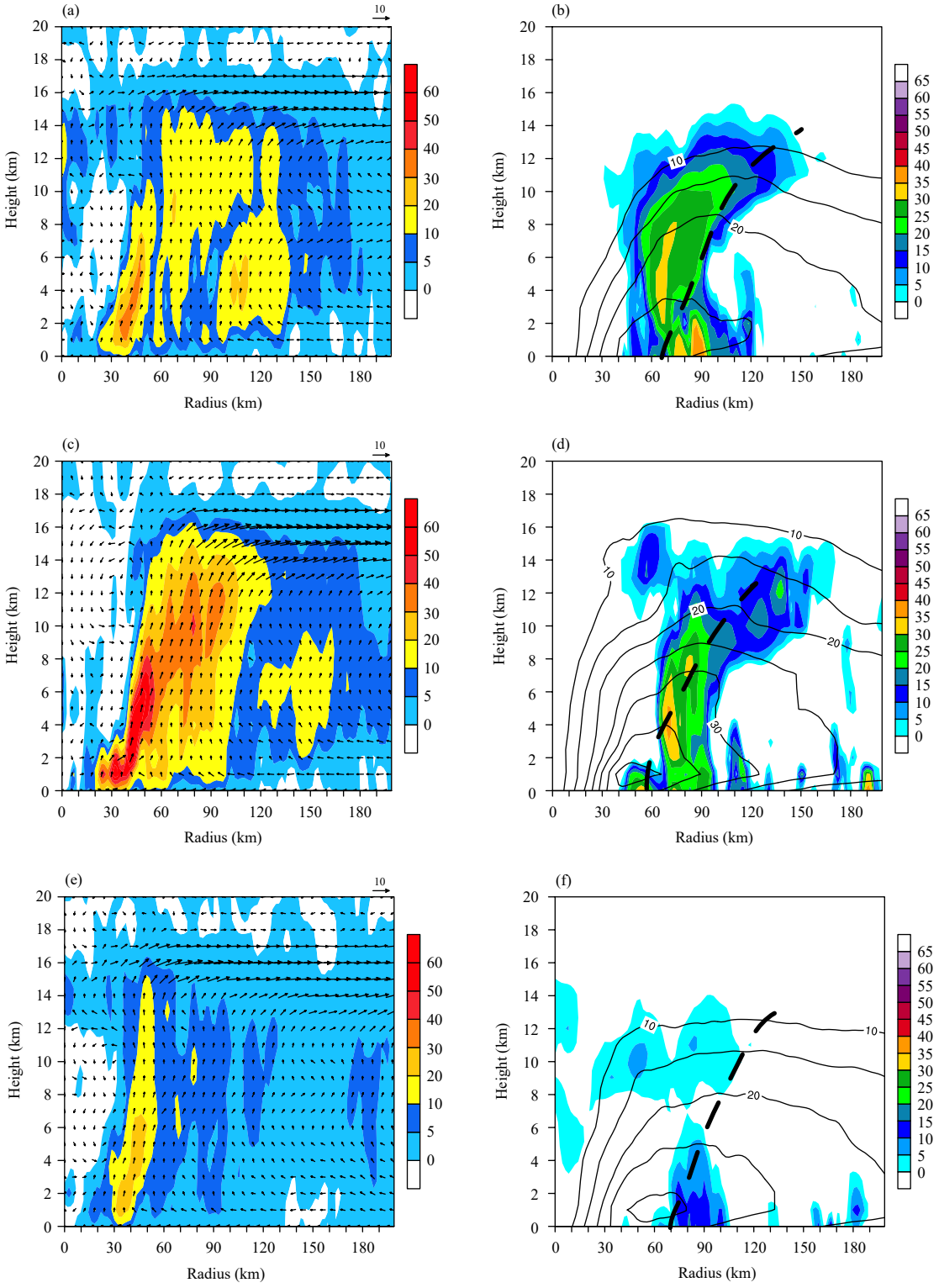

Fig. 13. Azimuthally and temporally averaged (a, c, e) vertical mass flux (shading; 10^8 kg s^{-1}) and secondary circulation (arrows; m s^{-1}), and (b, d, f) tangential wind (contours; m s^{-1}), RMW (black thick dashed line; km), and reflectivity (shading; dBZ), in the (a, b) control experiment, (c, d) NoSMLT experiment, and (e, f) NoIDEP experiment during the RI stage of Typhoon Hato.

demonstrates that the heating effect associated with the deposition of ice is critical to the RI of Hato. Besides, the other two sensitivity experiments (NoGMLT and NoIGEN) are also analyzed. The NoGMLT experiment shows similar mass flux and convection response features as the NoSMLT experiment, and the NoIGEN ex-

periment result is similar to that of the NoIDEP simulation (figures omitted).

8. Conclusions and discussion

In this study, the WRF-ARW (V3.8.1) model with a horizontal resolution of 2 km is used to investigate the RI of Typhoon Hato (2017). Overall, the model well reproduced the best-track surface maximum wind speed, sea surface pressure, and radar reflectivity. More specifically, the model can be used to simulate the TC track and intensity change well, especially during the process of RI, as well as the landfalling time and landfalling location. Besides, the simulated eyewall and rainband patterns are comparable to the observation in the inner-core region. Based on model outputs, cloud microphysical processes and their associated three-dimensional latent heating in the inner core of Hato are analyzed in detail. Moreover, their relative importance and contributions to the RI stage of Typhoon Hato are investigated.

From the viewpoint of cloud microphysical processes and their associated three-dimensional latent heating, in the RI stage, there is a significant increase of ice, snow, and graupel at levels between 8 and 12 km in the eyewall of Typhoon Hato. The total latent heating increases significantly with height from 0.5 to 15 km, which bears a close relationship with its RI. The positive latent heating or cooling under 0.5 km is dominated by water vapor evaporation. In the lower troposphere (0–4 km), water vapor condensation heating is the leading process, while deposition heating is dominant above 10 km. However, the heating composition between 4 and 10 km is complicated. Condensation, freezing, and deposition processes exist simultaneously, as does cooling from sublimation and melting. The total latent heating from all the processes combined plays significant roles in the structure and intensity changes of typhoon, particularly during the RI stage. After considering the contribution of each process, we find that water vapor condensation into cloud water contributes the largest positive latent heating (67.6%), followed by the depositional growth of ice (12.9%), and then the generation (nucleation) of ice from vapor (7.9%), similar to that shown for Typhoon Hagupit (Li et al., 2013a, b) and Meranti (Li et al., 2019). As for the cooling processes, the evaporation of rain is ranked in first place (47.6%), followed by the melting of snow to form cloud water (27.7%), and then the melting of graupel to form cloud water (9.8%). Based on the budget analysis, it may be helpful to pay special attention to cloud ice and snow deposition, as well as the generation (nucleation) processes, in the upper troposphere, when attempting to simulate the RI of a typhoon by numerical models with regard to the cloud microphysical parameterization scheme. Meanwhile, focus should also be given to the four main latent cooling processes in the middle and lower troposphere (especially between 5 and 6 km), which cause the total latent heat profile to decrease at those levels to some extent, similar to the inversion profile pattern. Sensitivity experiments further demonstrate that the intensification speed and the ultimate peak intensity are highly correlated with the dominant heating-effect microphysical processes, while the dominant cooling-effect ones have a relatively small impact on the RI and peak intensity. This suggests that improving the description of these large latent heating-associated processes in current cloud microphysical parameterization schemes is crucial to the numerical modeling of TC RI.

However, only a small number of microphysical schemes are tested, and thus some deficiencies still exist due to the microphysical parameterization scheme of a model. In fact, there are differences among the microphysics schemes in the WRF model package, and these might produce different results. Even with the WSM6 scheme used in their TC simulation, Li et al. (2013a, b) reproduced well the evolution of the intensity of Typhoon Hagupit (2008), while Ming et al. (2012) found less diabetic heating and weaker upward motion, and thus no RI, in simulating the evolution of the intensity of Super Typhoon Saomai (2006). Meanwhile, we are deeply aware of the complexity of the microphysical processes and their relationships with the evolution of TC intensity, especially RI. It is very important to reveal the underlying mechanisms of the different microphysical processes that impact upon RI from different aspects. Therefore, more simulations using different microphysical parameterization schemes and different cases are required in the future for a more detailed understanding of the mechanisms involved in the RI processes of typhoons. In forthcoming papers, we will focus on the physical relationship between latent heating and TC RI, and a detailed mechanistic study will be carried out.

Acknowledgments. We acknowledge the Shanghai Typhoon Institute, China Meteorological Administration for providing the best-track data at http://tcdata.typhoon.org.cn and NCEP of the US for providing the NCEP-FNL data at https://rda.ucar.edu/datasets/ds083.3.

REFERENCES

Anthes, R. A., 1982: *Tropical Cyclones: Their Evolution, Structure and Effects*. American Meteorological Society, Boston,

208 PP.

Bender, M. A., I. Ginis, and Y. Kurihara, 1993: Numerical simulations of tropical cyclone−ocean interaction with a high-resolution coupled model. *J. Geophys. Res. Atmos.*, **98**, 23245–23263, doi: 10.1029/93JD02370.

Cecelski, S., and D. L. Zhang, 2016: Genesis of Hurricane Julia (2010) within an African easterly wave: Sensitivity to ice microphysics. *J. Appl. Meteor. Climatol.*, **55**, 79–92, doi: 10.1175/JAMC-D-15-0105.1.

Cha, D. H., and Y. Q. Wang, 2013: A dynamical initialization scheme for real-time forecasts of tropical cyclones using the WRF Model. *Mon. Wea. Rev.*, **141**, 964–986, doi: 10.1175/MWR-D-12-00077.1.

Chen, H., and S. G. Gopalakrishnan, 2015: A study on the asymmetric rapid intensification of Hurricane Earl (2010) using the HWRF system. *J. Atmos. Sci.*, **72**, 531–550, doi: 10.1175/JAS-D-14-0097.1.

Chen, S. H., and W. Y. Sun, 2002: A one-dimensional time dependent cloud model. *J. Meteor. Soc. Japan*, **80**, 99–118, doi: 10.2151/jmsj.80.99.

Harnos, D. S., and S. W. Nesbitt, 2016: Varied pathways for simulated tropical cyclone rapid intensification. Part II: Vertical motion and cloud populations. *Quart. J. Roy. Meteor. Soc.*, **142**, 1832–1846, doi: 10.1002/qj.2778.

Heng, J. Y., Y. Q. Wang, and W. C. Zhou, 2017: Revisiting the balanced and unbalanced aspects of tropical cyclone intensification. *J. Atmos. Sci.*, **74**, 2575–2591, doi: 10.1175/JAS-D-17-0046.1.

Holliday, C. R., and A. H. Thompson, 1979: Climatological characteristics of rapidly intensifying typhoons. *Mon. Wea. Rev.*, **107**, 1022–1034, doi: 10.1175/1520-0493(1979)107<1022:CCORIT>2.0.CO;2.

Hong, S. Y., and J. O. J. Lim, 2006: The WRF single-moment 6-class microphysics scheme (WSM6). *J. Korean Meteor. Soc.*, **42**, 129–151.

Hong, S. Y., J. Dudhia, and S. H. Chen, 2004: A revised approach to ice microphysical processes for the bulk parameterization of clouds and precipitation. *Mon. Wea. Rev.*, **132**, 103–120, doi: 10.1175/1520-0493(2004)132<0103:ARATIM>2.0.CO;2.

Hong, S. Y., Y. Noh, and J. Dudhia, 2006: A new vertical diffusion package with an explicit treatment of entrainment processes. *Mon. Wea. Rev.*, **134**, 2318–2341, doi: 10.1175/MWR3199.1.

Houze Jr, R. A., 2010: Clouds in tropical cyclones. *Mon. Wea. Rev.*, **138**, 293–344, doi: 10.1175/2009MWR2989.1.

Iacono, M. J., J. S. Delamere, E. J. Mlawer, et al., 2008: Radiative forcing by long-lived greenhouse gases: Calculations with the AER radiative transfer models. *J. Geophys. Res. Atmos.*, **113**, D13103, doi: 10.1029/2008JD009944.

Kain, J. S., 2004: The Kain–Fritsch convective parameterization: An update. *J. Appl. Meteor.*, **43**, 170–181, doi: 10.1175/1520-0450(2004)043<0170:TKCPAU>2.0.CO;2.

Kaplan, J., and M. DeMaria, 2003: Large-scale characteristics of rapidly intensifying tropical cyclones in the North Atlantic basin. *Wea. Forecasting*, **18**, 1093–1108, doi: 10.1175/1520-0434(2003)018<1093:LCORIT>2.0.CO;2.

Kaplan, J., C. M. Rozoff, M. DeMaria, et al., 2015: Evaluating environmental impacts on tropical cyclone rapid intensification predictability utilizing statistical models. *Wea. Forecasting*, **30**, 1374–1396, doi: 10.1175/WAF-D-15-0032.1.

Lee, J. D., and C. C. Wu, 2018: The role of polygonal eyewalls in rapid intensification of typhoon Megi (2010). *J. Atmos. Sci.*, **75**, 4175–4199, doi: 10.1175/JAS-D-18-0100.1.

Leroux, M. D., M. Plu, D. Barbary, et al., 2013: Dynamical and physical processes leading to tropical cyclone intensification under upper-level trough forcing. *J. Atmos. Sci.*, **70**, 2547–2565, doi: 10.1175/JAS-D-12-0293.1.

Li, J. N., Wang, G., W. S., Lin, et al, 2013a: Cloud-scale simulation study of Typhoon Hagupit (2008) Part I: Microphysical processes of the inner core and three-dimensional structure of the latent heat budget. *Atmos. Res.*, **120-121**, 170–180, doi: 10.1016/j.atmosres.2012.08.015.

Li, J. N., Wang, G., W. S., Lin, et al, 2013b: Cloud-scale simulation study of Typhoon Hagupit (2008) Part II: Impact of cloud microphysical latent heat processes on typhoon intensity. *Atmos. Res.*, **120-121**, 202–215, doi: 10.1016/j.atmosres.2012.08.018.

Li, M. X., F. Ping, X. B. Tang, et al., 2019: Effects of microphysical processes on the rapid intensification of Super-Typhoon Meranti. *Atmos. Res.*, **219**, 77–94, doi: 10.1016/j.atmosres.2018.12.031.

Lin, I. I., C. H. Chen, I. F. Pun, et al., 2009: Warm ocean anomaly, air sea fluxes, and the rapid intensification of tropical cyclone Nargis (2008). *Geophys. Res. Lett.*, **36**, L03817, doi: 10.1029/2008GL035815.

Lin, Y. L., R. D. Farley, and H. D. Orville, 1983: Bulk parameterization of the snow field in a cloud model. *J. Climate Appl. Meteor.*, **22**, 1065–1092, doi: 10.1175/1520-0450(1983)022<1065:BPOTSF>2.0.CO;2.

Liu, H. Y., Y. Q. Wang, J. Xu, et al., 2018a: A dynamical initialization scheme for tropical cyclones under the influence of terrain. *Wea. Forecasting*, **33**, 641–659, doi: 10.1175/WAF-D-17-0139.1.

Liu, S., D. D. Tao, K. Zhao, et al., 2018b: Dynamics and predictability of the rapid intensification of Super Typhoon Usagi (2013). *J. Geophys. Res. Atmos.*, **123**, 7462–7481, doi: 10.1029/2018JD028561.

Liu, Y. B., D. L. Zhang, and M. K. Yau, 1997: A multiscale numerical study of Hurricane Andrew (1992). Part I: Explicit simulation and verification. *Mon. Wea. Rev.*, **125**, 3073–3093, doi: 10.1175/1520-0493(1997)125<3073:AMNSOH>2.0.CO;2.

Ma, Y. M., N. E. Davidson, Y. Xiao, et al., 2017: Revised parameterization of air–sea exchanges in high winds for operational numerical prediction: Impact on tropical cyclone track, intensity, and rapid intensification. *Wea. Forecasting*, **32**, 821–848, doi: 10.1175/WAF-D-15-0109.1.

Malkus, J. S., and H. Riehl, 1960: On the dynamics and energy transformations in steady-state hurricanes. *Tellus*, **12**, 1–20, doi: 10.3402/tellusa.v12i1.9351.

McFarquhar, G. M., B. F. Jewett, M. S. Gilmore, et al., 2012: Vertical velocity and microphysical distributions related to rapid intensification in a simulation of Hurricane Dennis (2005). *J. Atmos. Sci.*, **69**, 3515–3534, doi: 10.1175/JAS-D-12-016.1.

Miller, W., H. Chen, and D. L. Zhang, 2015: On the Rapid intensification of hurricane Wilma (2005). Part III: Effects of latent heat of fusion. *J. Atmos. Sci.*, **72**, 3829–3849, doi: 10.1175/JAS-D-14-0386.1.

Ming, J., S. J. Shu, Y. Wang, et al., 2012: Modeling rapid intensification of typhoon Saomai (2006) with the weather research and forecasting model and sensitivity to cloud microphysical parameterizations. *J. Meteor. Soc. Japan*, **90**, 771–789, doi: 10.2151/jmsj.2012-513.

Miyamoto, Y., and D. S. Nolan, 2018: Structural changes preceding rapid intensification in tropical cyclones as shown in a large ensemble of idealized simulations. *J. Atmos. Sci.*, **75**, 555–569, doi: 10.1175/JAS-D-17-0177.1.

Nolan, D. S., and L. D. Grasso, 2003: Nonhydrostatic, three-dimensional perturbations to balanced, hurricane-like vortices. Part II: Symmetric response and nonlinear simulations. *J. Atmos. Sci.*, **60**, 2717–2745, doi: 10.1175/1520-0469(2003)060<2717:NTPTBH>2.0.CO;2.

Nolan, D. S., Y. Moon, and D. P. Stern, 2007: Tropical cyclone intensification from asymmetric convection: Energetics and efficiency. *J. Atmos. Sci.*, **64**, 3377–3405, doi: 10.1175/JAS3988.1.

Pang, Q. Y., F. Ping, X. Y. Shen, et al., 2019: A comparative study of effects of different microphysics schemes on precipitation simulation for typhoon Mujigae (2015). *Chinese J. Atmos. Sci.*, **43**, 202–220, doi: 10.3878/j.issn.1006-9895.1804.17291. (in Chinese)

Qin, N. N., D. L. Zhang, W. Miller, et al., 2018: On the rapid intensification of Hurricane Wilma (2005). Part IV: Inner-core dynamics during the steady radius of maximum wind stage. *Quart. J. Roy. Meteor. Soc.*, **144**, 2508–2523, doi: 10.1002/qj.3339.

Rogers, R., 2010: Convective-scale structure and evolution during a high-resolution simulation of tropical cyclone rapid intensification. *J. Atmos. Sci.*, **67**, 44–70, doi: 10.1175/2009JAS3122.1.

Rogers, R., P. Reasor, and S. Lorsolo, 2013: Airborne Doppler observations of the inner-core structural differences between intensifying and steady-state tropical cyclones. *Mon. Wea. Rev.*, **141**, 2970–2991, doi: 10.1175/MWR-D-12-00357.1.

Rutledge, S. A., and P. Hobbs, 1983: The mesoscale and microscale structure and organization of clouds and precipitation in midlatitude cyclones. VIII: A model for the "Seeder-Feeder" process in warm-frontal rainbands. *J. Atmos. Sci.*, **40**, 1185–1206, doi: 10.1175/1520-0469(1983)040<1185:TMAMSA>2.0.CO;2.

Rutledge, S. A., and P. V. Hobbs, 1984: The mesoscale and microscale structure and organization of clouds and precipitation in midlatitude cyclones. XII: A diagnostic modeling study of precipitation development in narrow cold-frontal rainbands. *J. Atmos. Sci.*, **41**, 2949–2972, doi: 10.1175/1520-0469(1984)041<2949:TMAMSA>2.0.CO;2.

Schubert, W. H., and J. J. Hack, 1982: Inertial stability and tropical cyclone development. *J. Atmos. Sci.*, **39**, 1687–1697, doi: 10.1175/1520-0469(1982)039<1687:ISATCD>2.0.CO;2.

Tang, X. B., F. Ping, S. Yang, et al., 2018: Relationship between convective bursts and the rapid intensification of Typhoon Mujigae (2015). *Atmos. Sci. Lett.*, **19**, e811, doi: 10.1002/asl.811.

Tang, X. B., S. Yang, F. Ping, et al., 2019: Convection, latent heating and potential temperature budget in the rapidly intensifying Typhoon Mujigae (2015). *Atmos. Sci. Lett.*, **20**, e931, doi: 10.1002/asl.931.

Tao, C., H. Y. Jiang, and J. Zawislak, 2017: The relative importance of stratiform and convective rainfall in rapidly intensifying tropical cyclones. *Mon. Wea. Rev.*, **145**, 795–809, doi: 10.1175/MWR-D-16-0316.1.

Thompson, G., P. R. Field, R. M. Rasmussen, et al., 2008: Explicit forecasts of winter precipitation using an improved bulk microphysics scheme. Part II: Implementation of a new snow parameterization. *Mon. Wea. Rev.*, **136**, 5095–5115, doi: 10.1175/2008MWR2387.1.

Vigh, J. L., and W. H. Schubert, 2009: Rapid development of the tropical cyclone warm core. *J. Atmos. Sci.*, **66**, 3335–3350, doi: 10.1175/2009JAS3092.1.

Wang, H., and Y. Q. Wang, 2014: A numerical study of Typhoon Megi (2010). Part I: Rapid intensification. *Mon. Wea. Rev.*, **142**, 29–48, doi: 10.1175/MWR-D-13-00070.1.

Wang, Y., and C. C. Wu, 2004: Current understanding of tropical cyclone structure and intensity changes—A review. *Meteor. Atmos. Phys.*, **87**, 257–278, doi: 10.1007/s00703-003-0055-6.

Ying, M., W. Zhang, H. Yu, et al., 2014: An overview of the China Meteorological Administration tropical cyclone database. *J. Atmos. Oceanic Technol.*, **31**, 287–301, doi: 10.1175/JTECH-D-12-00119.1.

Yu, Y. B., and X. P. Yao, 2011: Thermodynamic characteristics of tropical cyclones with rapid intensity change over the coastal waters of China. *Acta Meteor. Sinica*, **25**, 467–477, doi: 10.1007/s13351-011-0407-y.

Zhu, T., and D. L. Zhang, 2006: Numerical simulation of Hurricane Bonnie (1998). Part II: Sensitivity to varying cloud microphysical processes. *J. Atmos. Sci.*, **63**, 109–126, doi: 10.1175/JAS3599.1.

Tech & Copy Editor: Hongqun ZHANG